

pubs.acs.org/acssensors Article

Standalone Stretchable Biophysical Sensing System Based on Laser Direct Write of Patterned Porous Graphene/Co₃O₄ Nanocomposites

Xiaohong Ding, Jin Xu, Jie Xu, Jinyun Zhao, Ruilai Liu, Longhui Zheng, Jun Wang, Yang Zhang, Zixiang Weng, Chen Zhang, Lixin Wu,* Huanyu Cheng,* and Cheng Zhang*



Cite This: ACS Sens. 2024, 9, 3730-3740



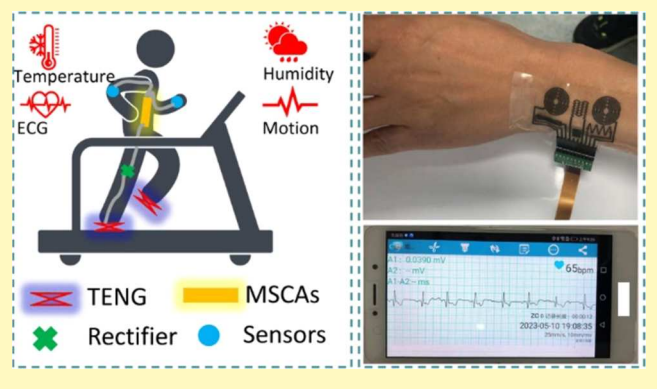
ACCESS I

III Metrics & More

Article Recommendations

sı Supporting Information

ABSTRACT: Skin-interfaced wearable sensors can continuously monitor various biophysical and biochemical signals for health monitoring and disease diagnostics. However, such devices are typically limited by unsatisfactory and unstable output performance of the power supplies under mechanical deformations and human movements. Furthermore, there is also a lack of a simple and cost-effective fabrication technique to fabricate and integrate varying materials in the device system. Herein, we report a fully integrated standalone stretchable biophysical sensing system by combining wearable biophysical sensors, triboelectric nanogenerator (TENG), microsupercapacitor arrays (MSCAs), power management circuits, and wireless transmission modules. All of the device components and interconnections based on the three-dimensional (3D)



networked graphene/ Co_3O_4 nanocomposites are fabricated via low-cost and scalable direct laser writing. The self-charging power units can efficiently harvest energy from body motion into a stable and adjustable voltage/current output to drive various biophysical sensors and wireless transmission modules for continuously capturing, processing, and wirelessly transmitting various signals in real-time. The novel material modification, device configuration, and system integration strategies provide a rapid and scalable route to the design and application of next-generation standalone stretchable sensing systems for health monitoring and human—machine interfaces.

KEYWORDS: triboelectric nanogenerator, microsupercapacitor arrays, biophysical sensors, graphene/ Co_3O_4 nanocomposites, standalone stretchable sensing systems

ighly integrated and miniaturized wearable sensing systems with seamless and conformal contact with human skin are essential to obtain accurate multimodal biosensing to continuously and noninvasively monitor human activities and health status in real-time. 1-3 The system needs to integrate wearable sensors with energy harvesters and suitable energy storage devices along with power management circuits and wireless transmission modules.4 However, soft, lightweight, sustainable, and safe power supplies are often less studied and developed due to the challenges of unsatisfactory and unstable output performance under mechanical deformation and human movements, especially during a long-term operation.^{5,6} In addition, these varying device components generally require the deposition of patterned functional micro/ nanomaterials (e.g., metallic or carbon nanomaterials, conducting polymers, or liquid metals) on soft substrates through arduous, time-consuming, high-cost, and complex manufacturing processes (e.g., photolithography, wet etching, and threedimensional (3D) printing). Therefore, it is highly desirable to develop an efficient, cost-effective, and scalable fabrication

method for fully integrated standalone stretchable sensing systems.

Readily patterned by irradiating carbon sources with a CO₂ laser, laser-induced porous graphene foams have recently been applied to electrocatalysis, soft actuators, sensors, and energy conversion and storage devices because of their mechanical robustness, excellent thermal and chemical stability, and high electrical conductivity. Additionally, surface modification of these porous graphene foams can further tune their physical, chemical, electronic, and optical properties for different target applications. More interestingly, it is possible to directly pattern hybrid nanocomposites by a second direct laser writing of nanoparticles (e.g., metal, alloys, and metal oxides/sulfides) on porous graphene foams. Meanwhile, transition metal oxide

Received: April 18, 2024 Revised: May 31, 2024 Accepted: June 18, 2024 Published: June 25, 2024





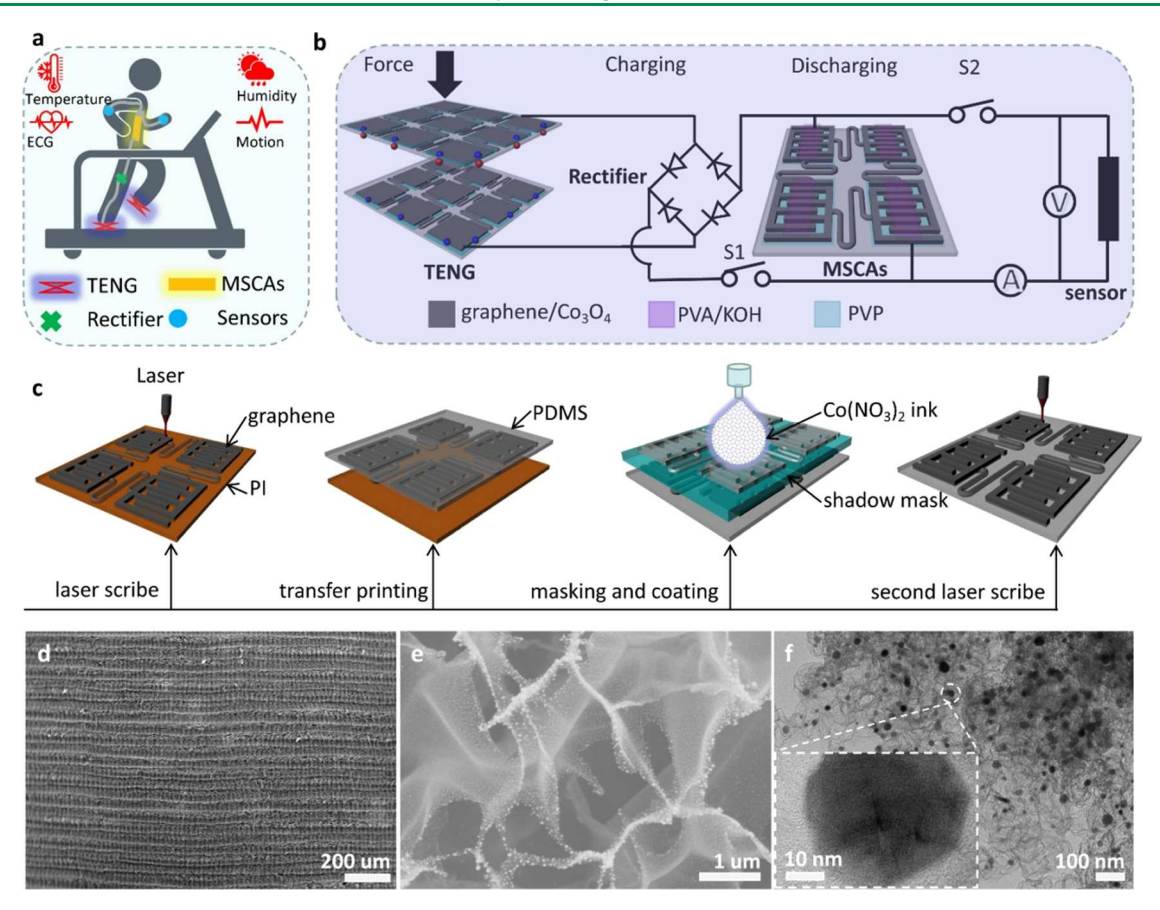


Figure 1. Design concept and structure of the stretchable self-charging power units to continuously drive wearable biophysical sensors. Schematic illustrating (a) the application of the standalone stretchable device system that integrates (b) self-charging power units consisting of triboelectric nanogenerators (TENG) and microsupercapacitor arrays (MSCAs) with on-skin sensors all based on laser-induced graphene foams decorated with Co_3O_4 nanocrystals (graphene/ Co_3O_4) for continuous, real-time monitoring of human physiological signals such as skin temperature, electrophysiology (ECG), skin humidity, arterial pulse, and body motion. (c) The fabrication process of the patterned graphene/ Co_3O_4 nanocomposite by a two-step laser direct writing process. (d) Low- and (e) High-magnification scanning electron microscopy (SEM) images and (f) transmission electron microscopy (TEM) images of the graphene/ Co_3O_4 nanocomposite.

nanostructures (e.g., MnO₂, RuO, Co₃O₄, Fe₃O₄) are broadly recognized as excellent active materials for wearable electronics because of their high redox activity, great reversibility, ease of chemical functionalization, and the potential mass production. The in situ formation of nanoparticles such as Co₃O₄ nanocrystals in porous graphene can simultaneously take advantage of the faradaic redox activity of the former and the capacitive 3D network of the latter to result in significantly improved kinetics and electrochemical performance at high rates. ^{13,14}

This work reports a rapid, low-cost, and scalable fabrication approach to directly create patterned graphene/Co₃O₄ nanocomposites for varying device components, resulting in a fully integrated standalone stretchable biophysical sensing system. The unique 3D network structure, together with the synergetic interaction between Co₃O₄ nanoparticles and graphene in the hybrid nanocomposites, provides energy harvesters, energy storage units, sensors, and signal processing circuits with excellent performance. The self-charging power units in the integrated system consist of the stretchable triboelectric nanogenerator (TENG), rectification circuit, and microsupercapacitor arrays (MSCAs). The self-charging power units can directly convert low-quality mechanical energy from human motions and activities into electricity and then store it as stable electrochemical energy to continuously power

wearable biophysical sensors and wireless transmission modules for real-time monitoring of health status. The fully integrated standalone stretchable sensing system can continuously capture, process, and wirelessly transmit skin temperature, electrophysiology (ECG), skin humidity, arterial pulse, and body motion for noninvasive and continuous health monitoring without an external power supply. The integrated system can also go beyond biophysical to biochemical to result in the next-generation standalone stretchable sensing system for wearable health monitoring, prosthetics and rehabilitation, and human—robot collaborations.

■ RESULTS AND DISCUSSION

Design of High-Performance Flexible Self-Charging Power Units. The flexible self-charging power units consist of a stretchable TENG and a stretchable MSCA based on graphene/Co₃O₄ nanocomposites (Figure 1a). The stretchable TENG mounted onto the shoe sole can harvest energy from human motions into electrical energy through coupled contact electrification and electrostatic induction between two oppositely surface-charged materials (see the working principle in Figure S1). With the help of a bridge rectifier, the intermittent impedance mismatch (high voltage but low current) and alternating current (AC) output electrical energy from TENG can be stored in stretchable MSCAs to yield a

controllable, stable, and continuous power supply. When fully charged, the output voltage/current of the MSCAs can be easily adjusted for target applications through series and/or parallel connections of multiple MSC devices. Thus, wearable biophysical sensors can be powered by flexible self-charging power units to monitor key physiological signals, including skin temperature, ECG, skin humidity, arterial pulse, and body motion (Figure 1b). The integration of all electronic device components on the same ultrathin and insulated elastomeric substrate (e.g., 100 μ m-thick plasma desorption mass spectrometry (PDMS)) yields a standalone stretchable system with seamless and conformal contact with human skin through a double-sided medical tape.

Advanced materials are crucial to preparing the key components in mass-producible, high-performance, and lowcost standalone stretchable device systems. The direct laser writing technique is maskless and cost-effective to synthesize and pattern a wide range of carbon-based nanomaterials and nanocomposites, including laser-induced graphene and its nanocomposites with metal and alloys such as metal oxides/ sulfides for wearable electronics. The graphene/Co₃O₄ nanocomposite with a 3D network is patterned to form the key components of all device components (i.e., TENG, MSCA, and on-skin biophysical sensors) and interconnections by a scalable and low-cost CO₂ laser scribing (Figure 1c). Briefly, the 3D networked graphene foam with designed geometric patterns is first transferred from the PI film to an ultrathin Ecoflex substrate with a thickness of 100 μ m. Next, the ink with Co(NO₃)₂ in deionized water, ethanol, and Nafion solution is spray-coated on the graphene foam using a shadow mask, followed by freeze-drying in a vacuum. Applying transient heating by the same CO2 laser then yields the 3D networked graphene/Co₃O₄ nanocomposite. The scalable, rapid, and low-cost manufacturing approach is promising for the future commercialization of graphene-based flexible/ stretchable electronics.

The morphology and structure of the graphene/Co₃O₄ nanocomposite are characterized by scanning electron microscopy (SEM), transmission electron microscopy (TEM), Raman spectroscopy, X-ray diffraction (XRD), X-ray photoelectron spectroscopy (XPS), and Kelvin probe force microscopy (KPFM). The graphene/Co₃O₄ nanocomposite exhibits a porous 3D networked microstructure due to the release of the gaseous products during the laser scribing of the PI film (Figure 1d), which can provide a high active surface area and short transport path for both electrons and ions. 15 Notably, nanoparticles are uniformly embedded in the graphene flakes (Figure 1e), likely attributed to the welldispersed spray ink in the hydrophilic graphene foam. The overall morphology of the graphene/Co₃O₄ nanocomposite is almost the same as that of laser-induced graphene foam (Figure S2). The TEM image shows that the graphene flakes with disordered grain boundaries and nanoparticles have a relatively uniform diameter size of ~50 nm (Figures 1f and S3). The XRD pattern of the graphene/Co₃O₄ nanocomposite (Figure S4a) shows that all featured diffraction peaks can be indexed to pure Co₃O₄ with the fluid catalytic cracking (FCC) structure (JCPDS No.42-1467)¹⁶ and laser-induced graphene. The XPS of graphene/Co₃O₄ nanocomposite (Figure S4bc) further confirms the chemical bonding between Co₃O₄ nanoparticles and the graphene foam by the featured peak of the Co-O-C bond at ~531.8 eV. 17 Additionally, the Raman spectrum of the nanocomposite (or graphene foam) (Figure

S4d) demonstrates that the G band (at 1580 cm⁻¹) is much higher than the two-dimensional (2D) band (at 2700 cm⁻¹) with an intensity ratio of 2.1 (or 2.0), respectively, indicating a few-layered structure in the graphene foam. Furthermore, the relatively low D/G intensity ratio of 0.69 indicates a high degree of graphene formation in the nanocomposite. Notably, the sheet resistance slightly reduces from 38 Ω/sq for the LIG foam to 32 Ω/sq for the graphene/Co₃O₄ nanocomposite, indicating high electrical conductivity. This sheet resistance value is smaller compared with previously reported LIG⁸ and LIG foams with Au nanocrystals¹⁹ due to higher thermal reduction temperature during the photothermal process at increased laser power used for the graphene/Co₃O₄ nanocomposite. As the laser power increases, a highly localized temperature rise from the photothermal process can lead to a high degree of graphitization, but partial oxidation reactions between graphene and oxygen molecules in ambient air start to occur, resulting in a negative effect on the quality of the films. Therefore, the resistance of graphene foam first gradually reduces to a minimum value (38 Ω/sq at 3.8 W) and then slowly increases to 41 Ω /sq at 5.2 W with increasing laser power. As a result, a laser power of 3.8 W is chosen for the highest conductivity in the following studies unless specified otherwise. The measurements with Kelvin probe force microscopy (KPFM) reveal the work function of LIG and graphene/Co₃O₄ nanocomposites to be ~4.0 and 2.3 eV, respectively. Therefore, the Co₃O₄ nanoparticles anchored on LIG foams affect the effective crystal potential as well as the Fermi level and work function to result in the work function difference between the two triboelectric materials for increased triboelectric charge density in TENG. Furthermore, the water contact angle measured by a contact angle measurement instrument (Figure S5) decreases from ca. 73° for LIG foams to 31° for the graphene/Co₃O₄ nanocomposite, which indicates drastically improved surface wettability. As a result, the graphene/Co₃O₄ nanocomposite exhibits an increased mass loading of active materials for faster redox reactions, contributing to enhanced electrochemical energy storage. The enhanced surface wettability with greatly improved electrical conductivity also promotes the adsorption of water molecules on the graphene/Co₃O₄-based humidity sensor for enhanced humidity sensing performance. Therefore, the laser direct writing of the graphene/Co₃O₄ nanocomposite with programmed geometries and high electrical conductivity provides a new class of materials for next-generation wearable electronics.

Design and Characterization of the Graphene/Co₃O₄ Nanocomposite-Based Wearable TENG. The graphene/ Co₃O₄ nanocomposite with rough and porous microstructures provides ultralarge active surface area and fast electronic/ion conducting channels for developing high-performance device components in the standalone stretchable system. The stretchable TENG features an electrode based on a graphene/Co₃O₄ nanocomposite with an island-bridge layout on a flexible PDMS film. To minimize the negative effect from environmental factors (such as water vapor, oxygen, and atmospheric pressure), the device is packaged with waterproof PDMS layers. By using a linear motor to apply the external force at varying frequencies, the interelectrode distance controlled by the PDMS layer thickness is optimized to be 4.0 mm for an external load of 1 M Ω . As the contact force increases from 20 to 100 N at 2.5 Hz, the output voltage increases from 69 to 120 V due to an increased effective

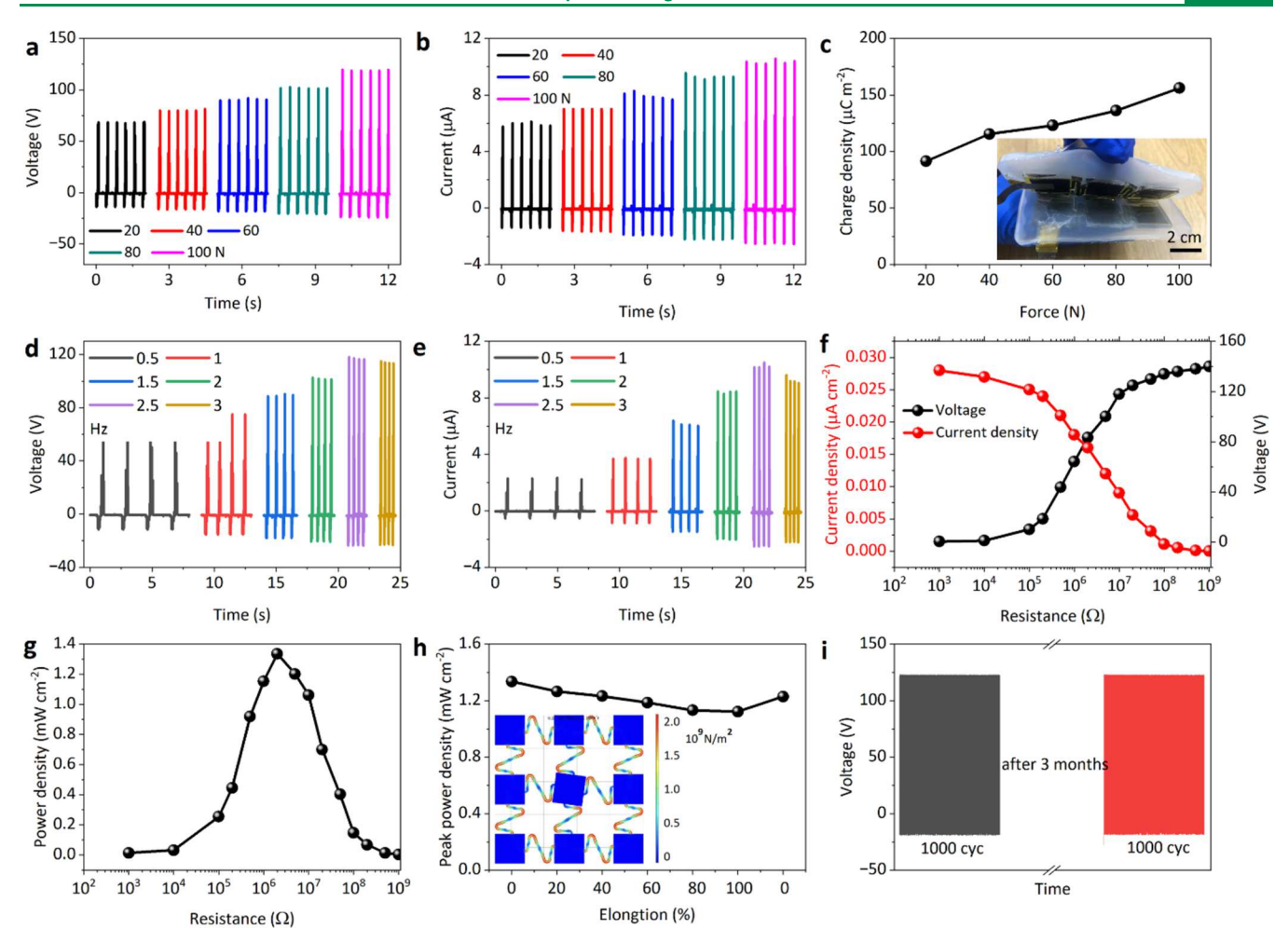


Figure 2. Design and characterization of the stretchable TENG. The measured output (a) voltage, (b) current density, and (c) charge density of the stretchable TENG as a function of the applied force from 20 to 100 N at a frequency of 2.5 Hz and a load resistance of 1 M Ω , with the optical image of the TENG shown in the inset. The measured output (d) voltage and (e) current density at various frequencies. (f) The output voltage, current density, and (g) power density of the TENG with different external load resistances for 100 N at 2.5 Hz. (h) Real-time output peak power density of the TENG upon stretching up to 100%, with the finite element analysis (FEA) of strain distribution in the graphene/ Co_3O_4 electrode under 100% elongation shown in the inset. (i) The long-term stability test of stretchable TENG over 3 months.

contact area for enhanced coupling effect of contact electrification (Figure 2a).²⁰ Meanwhile, the corresponding output current densities and transfer charge density also increase with an increase in force (Figure 2bc). As the loading frequency increases from 0.5 to 3 Hz, the peak output voltages and current densities first increase and then slightly decrease (Figure 2d,e). The initial increase results from more charge introduced at the higher frequency, whereas the slight decrease is likely attributed to the incomplete release of the transferred charge at the much faster mechanical deformation.²¹ In comparison, the output voltage and current density of the LIG-based TENG are only 98 V and 8 uA under a cycled compressive force of 100 N at a frequency of 2.5 Hz, with the decreased output performance attributed to the smaller work function difference between the LIG and PDMS electrodes (the work function difference between the two triboelectric materials in LIG- and graphene/Co₃O₄-based TENG are 2.5 and 4.2 eV, respectively). Evaluation of the power output of the graphene/Co₃O₄ nanocomposite-based TENG reveals an increased output voltage and decreased output current (Figure 2f) as the load resistance increases from 1 k Ω to 1 G Ω (100 N at 2.5 Hz), resulting in the maximum output power density of 1.34 mW cm⁻² at 2 M Ω (Figure 2g).

Besides high output characteristics, the TENG based on the graphene/Co₃O₄ nanocomposite with an island-bridge layout also features superior mechanical stretchability and durability. As the tensile strain increases from 0 to 100%, the output peak power density of the stretchable TENG exhibits a slight decrease to 84% of the initial value, which further recovers to 92% of the initial value after the release of the applied strain (Figure 2h). The slightly decreased output peak power density of the stretchable TENG with an island-bridge layout under elongation can be attributed to the increased resistance of the graphene/Co₃O₄ nanocomposite-based electrode, while the contact area of the TENG between the two membranes remains unchanged. The excellent output performance of the stretchable TENG under large tensile strains is likely attributed to the small peak principal strain of only 1.6% in the active square graphene/Co₃O₄ electrode islands for an applied tensile strain of 100% in finite element analysis (FEA) (Figure 2h, inset). The stretchable TENG based on the graphene/Co₃O₄ nanocomposite also exhibits superior long-term durability to remain at an output voltage of 120 V over 1000 cycles for 100 N at 2.5 Hz, even after exposing the TENG in the ambient environment for 3 months (Figure 2i). The excellent output performance and superior long-term durability of the

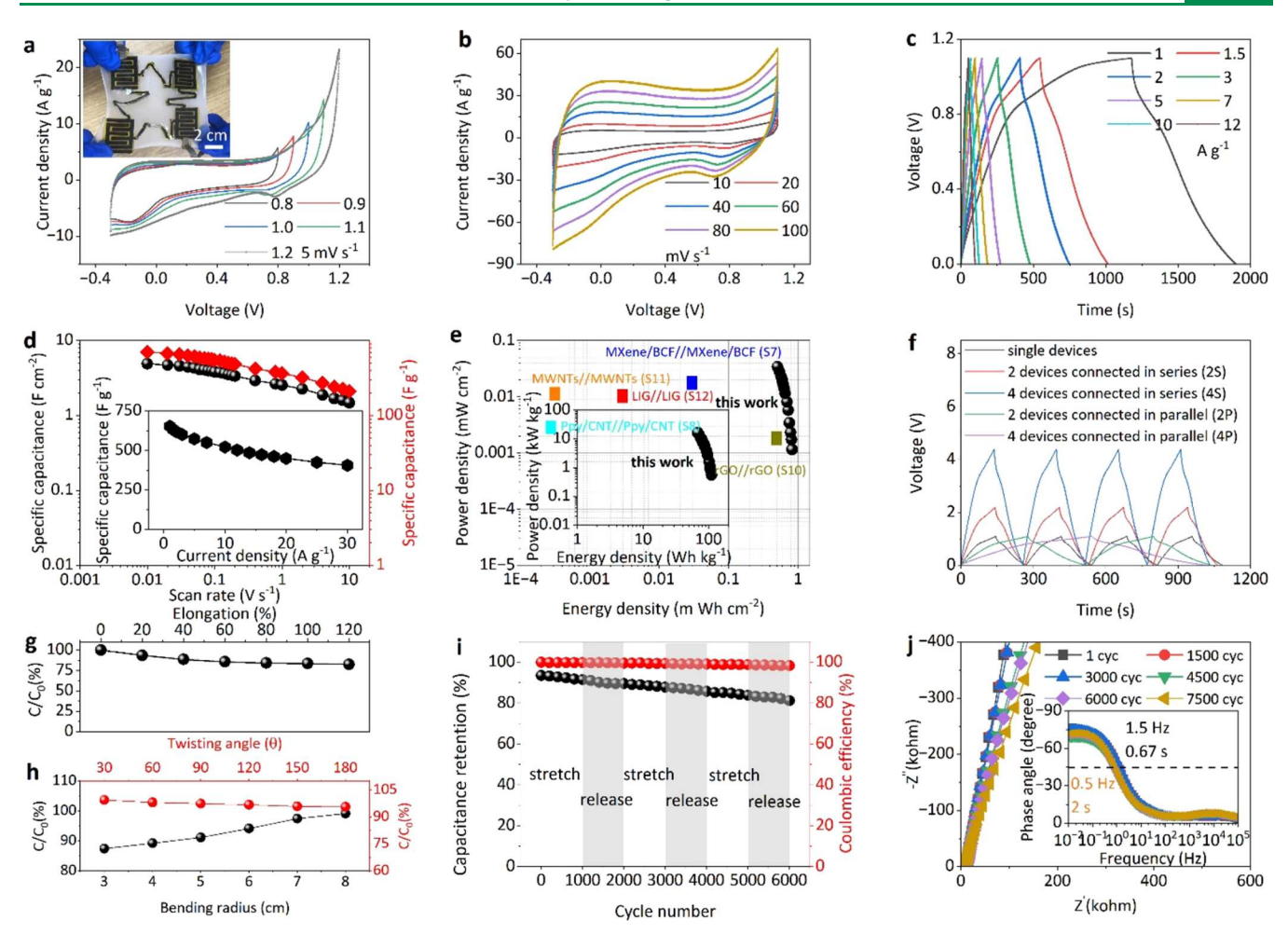


Figure 3. Design and characterization of the stretchable MSCAs based on the graphene/Co₃O₄ nanocomposite with an interdigitated electrode configuration. (a) Cyclic voltammogram (CV) curves of MSC with different voltage windows at a scan rate of 5 mV·s⁻¹, with an optical image of the stretchable MSCAs shown in the inset. (b) CV curves of the MSC in the stable potential window from -0.3 to 1.1 V at different scan rates. (c) Galvanostatic charge–discharge (GCD) curves of the MSC at different current densities in the potential window of 1.1 V. (d) Specific capacitance of the MSC calculated from the GCD curves with different scan rates and current densities. (e) Power and energy densities in the Ragone plot compared with those reported in the literature. (f) GCD curves of the MSCAs with serial and/or parallel connections at a current density of 5 A g⁻¹. The normalized capacitance retention of the MSCAs with four MSC cells interconnected in parallel versus b(g) stretching and (h) twisting/bending deformations. (i) Capacitance retention and Coulombic efficiency of the MSCAs during 6000 charge–discharge cycles. (j) Electrochemical impedance spectra (EIS) of the MSC over 75,000 charge–discharge cycles, with the bode plots of phase angle versus frequency shown in the inset.

stretchable TENG based on the graphene/ Co_3O_4 nanocomposite from a scalable and cost-effective fabrication approach outperforms the previously reported carbon-based wearable TENGs (Table S1).

Design and Characterization of the Graphene/Co₃O₄ Nanocomposite-Based MSCAs. The graphene/Co₃O₄ nanocomposite with a 3D network structure and high surface area can also provide capacitive and faradaic energy storage to store the harvested electrical energy in MSCAs. A highly flexible and stretchable all-in-one MSCA configured in the islands-bridge layout is easily fabricated at a large scale by coating the PVA/KOH ionic gel electrolyte on the coplanar interdigitated electrodes (Figure 3a, inset). The characterization of the resulting MSC cells with cyclic voltammetry (CV) indicates a stable electrochemical window of 1.1 V at a scan rate of 5 mV s⁻¹ (Figure 3a). The CV curves at different scan rates from 10 to 100 mV s⁻¹ display faradaic pseudocapacitive shape according to the redox peaks (Figure 3b), suggesting outstanding pseudocapacitive performance and

fast charge-discharge properties.²² This excellent capacitive behavior is further confirmed by the galvanostatic chargedischarge (GCD) curves at varying current densities from 1 to 12 A g⁻¹ (Figure 3c). Specifically, pronounced plateaus observed in the charge-discharge process, even at a high current density of 3 A g⁻¹, confirm the pseudocapacitive characteristics derived from faradaic redox reactions. The GCD curves of the graphene/Co₃O₄ nanocomposite-based MSC further indicate excellent rate capability and an impressive gravimetric capacitance of 654, 601, 574, 550, 522, 450, and 405 F g^{-1} at current densities of 1, 3, 5, 7, 10, 20, and 30 A g^{-1} , respectively (Figure 3d). Additionally, the specific areal (gravimetric) capacitance of the MSC increases from 1.48 F cm^{-2} (212 F g^{-1}) to 4.93 F cm^{-2} (704 F g^{-1}) as the scan rate is decreased from 10,000 to 10 mV s⁻¹. In comparison, the CV curves of LIG-based MSC at different scan rates (10-100 mV s⁻¹) exhibit typical quasi-rectangular shapes (Figure S6a) to indicate nearly ideal capacitive behavior. The increased current density with increasing scan rate indicates a low internal

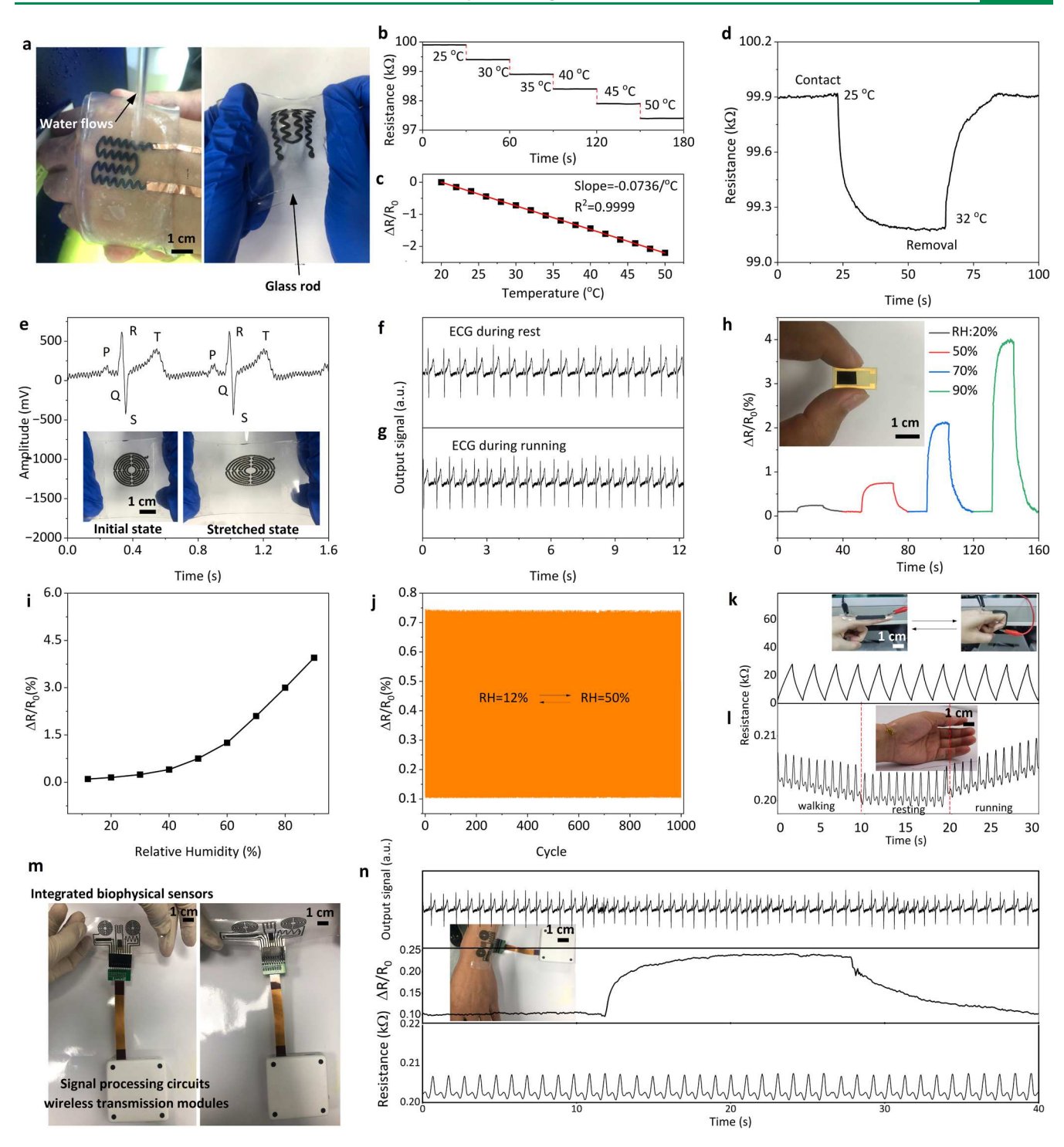


Figure 4. Design and characterization of wearable biophysical sensors based on the graphene/ Co_3O_4 nanocomposite. (a) Optical images of the nanocomposite-based temperature sensor on human skin under running water with a velocity of $3 \text{ m} \cdot \text{s}^{-1}$ (left) or being poked by a glass rod with a radius of curvature of 700 μm (right). (b) Dynamic response and (c) calibration plot of the temperature sensor. (d) Dynamic response of the wearable temperature sensor upon contact and removal from the skin (room temperature of $25 \,^{\circ}\text{C}$). (e) Electrocardiogram (ECG) signals collected from the wireless ECG sensing system with electrodes based on the graphene/ Co_3O_4 nanocomposite, with insets showing the optical images of the electrode before and after stretching. Comparison of ECG signals measured during (f) rest and (g) exercise. (h) Real-time sensing response of the humidity sensor to the relative humidity (RH) of 20, 50, 70, and 90%, with the optical image of the humidity sensor shown in the inset. (i) The calibration curve of the humidity sensor in the RH range from 12 to 90%. (j) The cyclic test of the humidity sensor between 12 and 50% over 1000 cycles. The output resistance change of the strain sensor (k) on the finger to detect bending and (l) on the arm to detect the pulse under resting, walking, and running, with an optical image of the pulse sensor on the wrist shown in the inset. (m) Optical images of the integrated biophysical sensors based on the graphene/ Co_3O_4 nanocomposite before (left) and after (right) 100% stretching. (n) Output characteristics of ECG (top), RH (middle), and pulse (bottom) signals from the integrated biophysical sensors on the wrist.

resistance and a high rate capability performance. Furthermore, the specific areal (gravimetric) capacitance of the MSC increases from 0.12 F cm⁻² (98 F g⁻¹) to 0.13 cm⁻² (108 F g⁻¹) as the scan rate is decreased from 100 to 10 mV s⁻¹ (Figure S6c). These values are much smaller than those of the graphene/Co₃O₄-based MSC, likely resulting from the single capacitive energy storage mechanisms in the LIG-based electrode. The graphene/Co₃O₄ nanocomposite-based MSC shows much superior performance when compared with the previous reports on carbon-based solid-state MSCs at similar scan rates, including porous laser-induced graphene of 1 mF cm $^{-2}$ (120 F g $^{-1}$) at 10 000 mV s $^{-18}$ holey graphene frameworks of 298 F g $^{-1}$ at 1 A g $^{-1}$; 23 crumpled porous graphene/MXene of 2.9 mF cm⁻² at 30 mA cm⁻²;²⁴ PANi/PVA of 367 F g⁻¹ at 2 mA cm⁻²;²⁵ and nanoporous gold/MnO₂ films of 601 F g⁻¹ at 0.3 A g⁻¹. Furthermore, the overall performance of the MSC in the Ragone plot also features high gravimetric energy density and power density of 109.91/101.01/96.46/87.73/75.63/68.14 Wh kg⁻¹ (or 0.83/0.76/0.73/0.66/0.57/0.51 mWh cm⁻²) and 0.55/1.65/2.75/5.50/11.03/16.52 kW kg⁻¹ (1.15/3.45/5.78/11.49/23.03/ 34.30 μ W cm⁻²) at 1/3/5/10/20/30 A g⁻¹, respectively (Figure 3e). The combined high energy and power densities are comparable to or even higher than those of other graphenebased MSCs previously reported (Table S2).

Connecting different numbers of nanocomposite-based MSCs in parallel (P) and/or series (S) with an islands-bridge layout results in stretchable MSCAs to drive wearable devices with varying power consumption needs. Compared with a single MSC with an operating voltage of 1.1 V, the MSCAs connected in serial configurations such as 2S and 4S can achieve voltages of 2.2 and 4.4 V with almost identical pseudocapacitive behaviors and discharge times (Figure 3f). Moreover, the output current and discharge time of the MSCAs in parallel linearly scale with the number of MSC cells.

The island-bridge architecture in MSCAs also allows out-of-plane buckling and twisting to accommodate mechanical deformation. The normalized capacitance retention (C/C_0) of MSCAs with four MSC cells interconnected in parallel decreases with the increasing tensile strain, and it still achieves 82.5% for a large tensile strain of 120% (Figure 3g). The MSCAs also exhibit robust performance against bending and twisting, with a capacitance loss of 0.4/1.8/2.4/3.2/4.0/4.3% upon twisting to $30/60/90/120/150/180^\circ$. Moreover, there is a slight decrease of 11.7% as the bending radius of curvature decreases from 8 to 3 cm (Figure 3h).

The cycling stability of the MSCAs with four MSC cells interconnected in parallel is highlighted by exhibiting only 18.7% loss in the specific capacitance after 6000 cycles obtained from the GCD analysis at 2 A g⁻¹ within 0-1.1 V (Figure 3i). Furthermore, the Coulombic efficiency is close to 100% after 6000 cycles, which is attributed to the reversible redox reactions on the surface of the Co₃O₄ nanoparticles.²⁷ Meanwhile, the electrochemical impedance spectroscopy (EIS) curves (after 1/1500/3000/4500/6000/7500 cycles) of the MSC in the frequency range of 100 kHz-0.01 Hz show a similar trend, with a semicircle in the higher frequency region (Figure S7) and an inclined line at a lower frequency (Figure 3j). The EIS analysis further demonstrates the low total resistance (from the electrodes, electrolyte, and contact) and excellent electrochemical stability.²⁸ The graphene/Co₃O₄ nanocomposite with well-retained overall morphology after 6000 charge-discharge cycles also indicates good cycling stability (Figure S8). The excellent electrochemical stability is likely attributed to the thin layer of PDMS encapsulation, which can protect the electrodes and gel electrolytes from exposure to the environment. Furthermore, the phase angles of MSCAs after 1/1500/3000/4500/6000/7500 cycles are close to -90° at low frequencies, and the characteristic frequency f_0 (at the phase angle of -45°) is about 1 Hz (Figure 3j, inset), indicating excellent electrochemical stability and high ion diffusion rate.²⁹

Sensing Characteristics of the Graphene/Co₃O₄ Nanocomposite-Based Wearable Biophysical Sensors. The unique physical and chemical properties of the graphene/ Co₃O₄ nanocomposite also afford high-performance biophysical sensors to detect skin temperature, ECG, skin humidity, arterial pulse, and body motion in real-time for medical diagnosis and health monitoring. A relatively rigid polyethylene terephthalate (PET) film is placed between the graphene/ Co₃O₄ nanocomposite and stretchable substrate to provide strain isolation, which helps reduce the strain effect for enhanced stability and accuracy of the measurements upon stretching. To continuously monitor skin temperature with high sensitivity, fast responses, and environmental stability, the wavy graphene/Co₃O₄ nanocomposite as a temperature sensing layer is wrapped in PDMS to interface with the skin by using a biocompatible liquid bandage (Nexcare, 3M). Besides seamless and conformal contact with the rough skin surface, the temperature sensor can withstand running water flow at a high velocity of 3 m $\rm s^{-1}$ or poking by a glass rod (Figure 4a). The excellent environmental stability of the graphene/Co₃O₄ nanocomposite-based wearable temperature sensor can be attributed to the packaging with highly stretchable waterproof PDMS layers and the direct growth of Co₃O₄ nanoparticles on the flexible 3D porous graphene scaffold. Modulated by the electron-phonon scattering and thermal velocity of electrons, the conductivity of the graphene/ Co₃O₄ nanocomposite increases with increasing temperature in the range from 20 to 50 °C (Figure 4c). The measured temperatures in the range from 20 to 50 °C are consistent with those measured by a commercial thermometer (Deli, LE505) (Figure S9). The slope of the calibration plot gives the sensitivity of 0.074% $^{\circ}$ C¹⁻ according to $S = |R - R_0| \times 100/$ $(R_0 \times \Delta T)$, where R and R_0 are the temperature-dependent and initial resistances, respectively, and ΔT is the temperature variation (Figure 4c).30 The linear fit also gives the limit of detection (LOD) of 0.042 °C, estimated from LOD = $3\sigma/S$, where σ is the standard deviation. A fast response with full recovery is observed when the sensor in the room is brought into contact with and removed from the skin (Figure 4d). The response time of the temperature sensor is fundamentally determined by the thermal conductivity of the encapsulation material, so it is possible to reduce the response time by using ultrathin encapsulation materials with high thermal conductivity. In summary, the conformal temperature sensor shows high sensitivity, an ultralow detection limit, and quick response even under dynamic deformations.

A real-time, continuous monitoring of ECG signals can provide insights into the electrical changes associated with heart muscle depolarization to alert for various diseases such as arrhythmias, pulmonary hypertension, or cardiac diseases.³¹ Integrating two stretchable ripple-like electrodes based on the graphene/Co₃O₄ nanocomposite with a commercial ECG sensing chip (ER1, Lepu Devices Inc.) and a Bluetooth module (CC2541, Guyu Link Inc.) yields an ECG sensing system on

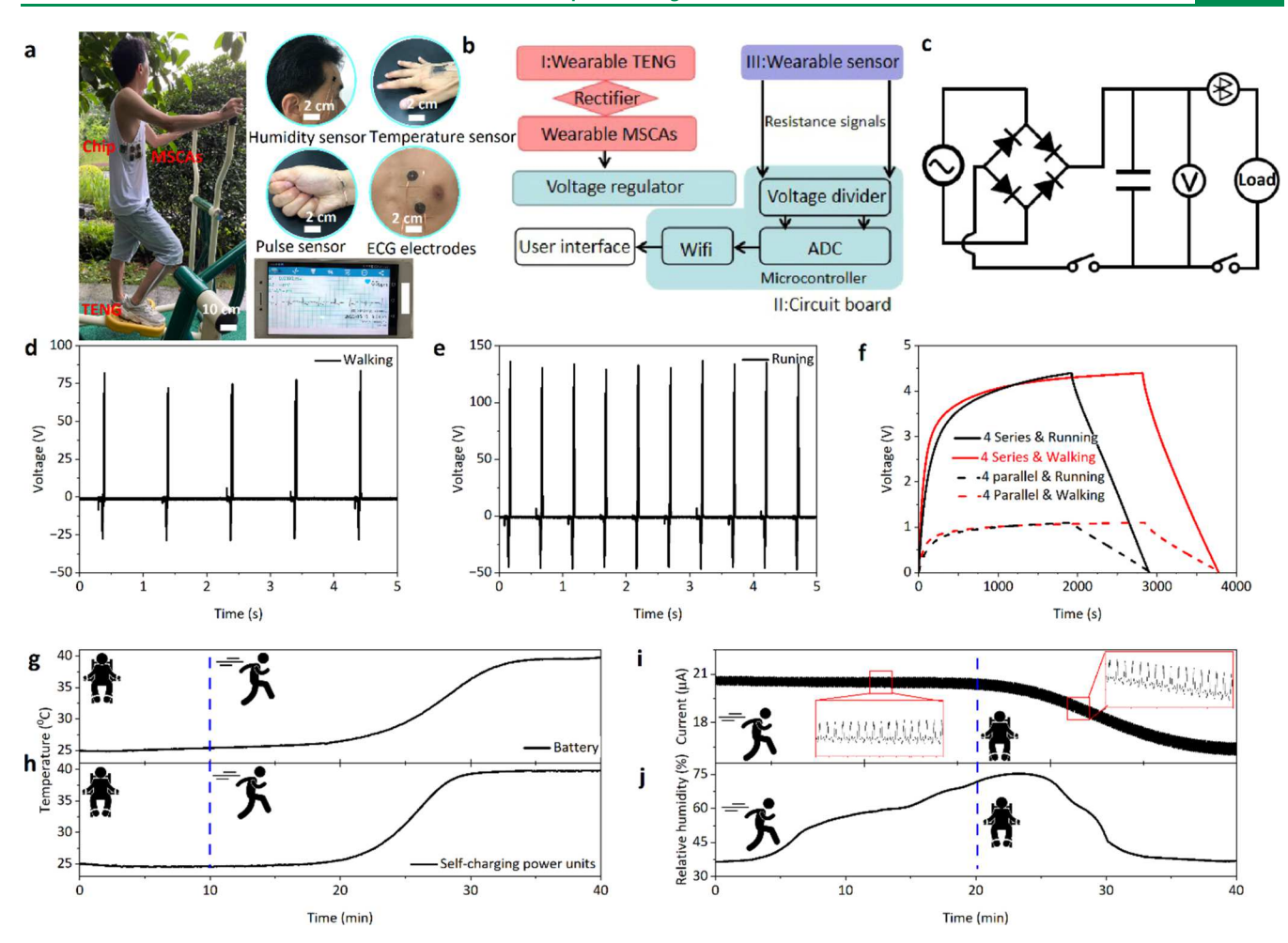


Figure 5. On-body evaluation of the fully integrated standalone biophysical sensing system for noninvasive and continuous health monitoring. (a) Photographs, (b) block diagram, and (c) circuit diagram of the fully integrated standalone biophysical sensing system attached to varying locations of the human skin. The output voltage of the graphene/ Co_3O_4 -based TENG shoe sole was driven by a human subject with a body weight of 80 kg under (d) walking and (e) running for 30 min. (f) The real-time potential of the MSCAs with four MSC cells interconnected in series and parallel charged by the insole TENG (discharge at 10 μ A). Real-time, continuous measurement of temperature driven by a (g) battery and (h) self-charging power unit, (i) pulse, and (j) skin humidity of a healthy human subject during running and sitting.

the chest (Figure S10), validated by the commercial ECG sensor (ECG-3303B, Figure S11). The two stretchable ECG electrodes are conformally attached to the chest with a biocompatible liquid bandage (Nexcare, 3M). Besides characteristic PQRST peaks (Figure 4e), the conformal ECG sensing system can also accurately and continuously measure ECG signals during rest (Figure 4f) and running (Figure 4g), with the heart rate (HR) increased from 78 to 118 beats/min. The signal-to-noise ratio (SNR) also only slightly decreases from 39.5 for resting to 32.3 dB for running according to SNR = 20 $\times \log(V_{\rm rmsl}/V_{\rm rmsn})$, where $V_{\rm rmsl}$ and $V_{\rm rmsn}$ are the rootmean-square values of the ECG signal without and with the noise, respectively.³² ECG signals can also be captured with graphene foam-based electrodes but with a reduced SNR of 28.5 dB for running due to undesirable adhere to human skin over long-term wear (Figure S12).

As a first step to detect biomarkers in sensible and insensible sweat, the skin humidity sensor can interface with the skin via a biocompatible liquid bandage (Nexcare, 3M). A waterproof but gas-permeable porous PDMS membrane prepared on the surface of the sensing components provides an effective diffusion pathway for water vapors while repelling liquid sweat. 33,34 The rapid adsorption and desorption of water

molecules on the surface of the graphene/Co3O4 nanocomposite change the sensor resistance over a wide range of relative humidity (RH) levels from 10 to 90% (Figure 4h), which agrees with those measured by a commercial humidity sensor (Delixi, DM-1043, Figure S13). The piecewise linear dependence of the sensitivity $S = |R - R_0| \times 100/R_0$ on RH shows a much higher value of 0.09 in RH 60-90% ($R^2 = 0.99$) than that of 0.01 ($R^2 = 0.96$) in RH 10-40% (Figure 4i). In comparison, the sensitivity of the LIG-based humidity sensor is only 0.03 in RH 60–90% ($R^2 = 0.98$) and 0.002 ($R^2 = 0.98$) in RH 10-40% (Figure S14), which can be attributed to the poor surface wettability and electrical conductivity of LIG. The flexible humidity sensor also shows a stable response with negligible changes over 1000 cycles between RH 12 and 50% (Figure 4j), suggesting a potential use for long-term operation. Furthermore, the piezoresistive pressure sensor based on the graphene/Co₃O₄ nanocomposite can clearly detect finger bending and arterial pulse from the human wrist (Figure 4k) even upon walking and running (Figure 41). The simultaneous recording of pulse and ECG signals on the wrists can further cufflessly detect the blood pressure using a pulse transit time method.³⁵ The measured diastolic/systolic blood pressure of a healthy human subject slightly increases from 75/119 at rest to

79/125 mmHg during walking, which is consistent with those measured by a commercial sphygmomanometer (Omron, J760, Figure S15). It should be noted that all of these biophysical sensors integrated on a single substrate (Figure 4m) exhibit almost unchanged sensing performance compared with the individual sensors (Figure 4n).

On-Body Evaluation of the Integrated Device System for Human Health Monitoring. As a proof-of-concept demonstration, a fully integrated standalone biophysical sensing system can seamlessly and stably interface with different locations of human skin or clothing for noninvasive, continuous, and wireless monitoring of human health status (Figure 5a). The kinetic energy from various exercises (e.g., walking, running, jogging, etc.) is first converted into electrical energy by the graphene/Co₃O₄-based insole TENG and then stored as electrochemical energy in the nanocomposite-based MSCAs using a bridge rectifier. The integrated TENG and MSCAs can serve as sustainable self-charging power units to drive biosensors and wireless transmission modules (Figure 5b,c). The output performance of the insole TENG driven by body motion with a body weight of 80 kg increases from walking (at a constant speed of 4 km h⁻¹) (Figure 5d) to running (9 km h⁻¹) to give an output voltage of 134 V and a maximum output power density of 1.26 mW cm⁻² at 2 M Ω (Figure 5e). The real-time potential of the MSCAs with four MSC cells interconnected in series/parallel charge by the insole TENG driven by walking at 4 km h⁻¹ and running at 9 km h⁻¹ first rapidly and then slowly increases to an operating voltage of 4.4/1.1 V for MSCAs with series/parallel connections (Figure 5f). The rapid charging of 1920/1875 s for the MSCAs with four MSC cells interconnected in series/ parallel during running at 9 km h⁻¹ (or 2817/2795 s during walking) is followed by almost linear discharging of 988/980 (or 963/972 s) at 10 μ A for stable power output. These results demonstrate that wearable self-charging power units can efficiently harvest and store energy with an adjustable and stable output performance for varying target applications. The running on a machine at 9 km h⁻¹ is chosen in the subsequent on-body testing unless specified otherwise.

The self-charging power unit can continuously drive the skin temperature, ECG, pulse, and skin humidity for human health monitoring. The wearable self-charging power units can either be continuously charged by the human subject with a body weight of 80 kg running at 9 km h⁻¹ (mode I) or simply act as a standalone power supply after charging (mode II). The flexible temperature sensor attached to the back of the hand shows comparable sensing performance between those powered by the battery (Figure 5g) and the wearable selfcharging power units over sedentary (mode II) and running states (mode I) (Figure 5h). Both temperature measurements are consistent with the value measured by a commercial thermometer (Deli, LE505). With the help of low-pass filter and smoothing algorithms, both arterial pulse (Figure 5i) and skin humidity (Figure 5j) can be wirelessly and continuously monitored by the pulse and humidity sensors powered by selfcharging power units. Despite the short monitoring time of 20 min and a gradual decrease in the base current of the pulse signals in the sedentary state (mode II), continuous monitoring is possible with the integrated self-charging power units operated in mode I (Figure 5i). At the same time, the wearable self-charging electrophysiological sensing system also accurately measures the surface ECG signals (Figure S16) and wirelessly transmits the data to the

smartphone (Figure 5a, bottom). The standalone biophysical sensing system can maintain superior stretchability, stability, and reasonably good sensing performance even when exposed to the ambient environment for 3 months (Figure S17). The performance could be further improved with durable encapsulation layers for use in practical applications.

CONCLUSIONS

In summary, this work demonstrated a fully integrated standalone wearable biophysical sensing system that combines wearable TENG, MSCAs, biophysical sensors, power management circuits, and wireless transmission modules for health monitoring. All of the device components and interconnections based on patterned graphene/Co₃O₄ nanocomposites were fabricated by a low-cost and scalable laser fabrication method. The facile integration with commercial off-the-shelf (COTS) chips, such as microcontroller and wireless modules, further extended the application opportunities for the integrated device system. The demonstrated standalone stretchable sensing system can continuously capture, process, and wirelessly transmit skin temperature, ECG, humidity, pulse, and body motion in real-time. The demonstrated design, fabrication, and integration can result in the next-generation standalone stretchable biophysical and biochemical monitoring platforms for human-computer interaction, smart soft robots, and an intelligent Internet of Things.

ASSOCIATED CONTENT

Supporting Information

The Supporting Information is available free of charge at https://pubs.acs.org/doi/10.1021/acssensors.4c00916.

Experimental section; schematic showing the working principle of graphene/ Co_3O_4 nanocomposite-based TENG under cyclic compressive force; SEM, TEM, XRD, XPS, and Raman of 3D LIG foams and graphene/ Co_3O_4 nanocomposites; water droplet on the surface of 3D LIG foams and graphene/ Co_3O_4 nanocomposites; electrochemical characterization of LIG-based MSC; the comparison of sensing signals measured between graphene/ Co_3O_4 -based electrodes and the commercial sensor; the stability test of the standalone biophysical sensing system (PDF)

AUTHOR INFORMATION

Corresponding Authors

Lixin Wu − CAS Key Laboratory of Design and Assembly of Functional Nanostructures, Fujian Key Laboratory of Nanomaterials, Fujian Institute of Research on the Structure of Matter, Chinese Academy of Sciences, Fuzhou 350002, China; orcid.org/0000-0002-4616-0283; Email: lxwu@fjirsm.ac.cn

Huanyu Cheng — Department of Engineering Science and Mechanics, Materials Research Institute, Pennsylvania State University, University Park, Pennsylvania 16802, United States; orcid.org/0000-0001-6075-4208; Email: huanyu.cheng@psu.edu

Cheng Zhang — Fujian Key Laboratory of Functional Marine Sensing Materials, College of Material and Chemical Engineering, Minjiang University, Fuzhou 350108, P. R. China; Department of Engineering Science and Mechanics, Materials Research Institute, Pennsylvania State University, University Park, Pennsylvania 16802, United States; orcid.org/0000-0001-5810-9680; Email: zhangcheng@mju.edu.cn

Authors

- Xiaohong Ding Fujian Provincial Key Laboratory of EcoIndustrial Green Technology, College of Ecological and
 Resources Engineering, Wuyi University, Wuyishan 354300,
 P. R. China; Fujian Key Laboratory of Functional Marine
 Sensing Materials, College of Material and Chemical
 Engineering, Minjiang University, Fuzhou 350108, P. R.
 China; Department of Engineering Science and Mechanics,
 Materials Research Institute, Pennsylvania State University,
 University Park, Pennsylvania 16802, United States; CAS
 Key Laboratory of Design and Assembly of Functional
 Nanostructures, Fujian Key Laboratory of Nanomaterials,
 Fujian Institute of Research on the Structure of Matter,
 Chinese Academy of Sciences, Fuzhou 350002, China;
 orcid.org/0000-0002-9693-2691
- Jin Xu Fujian Provincial Key Laboratory of Eco-Industrial Green Technology, College of Ecological and Resources Engineering, Wuyi University, Wuyishan 354300, P. R. China
- Jie Xu Fujian Provincial Key Laboratory of Eco-Industrial Green Technology, College of Ecological and Resources Engineering, Wuyi University, Wuyishan 354300, P. R. China
- Jinyun Zhao Fujian Provincial Key Laboratory of Eco-Industrial Green Technology, College of Ecological and Resources Engineering, Wuyi University, Wuyishan 354300, P. R. China
- Ruilai Liu Fujian Provincial Key Laboratory of Eco-Industrial Green Technology, College of Ecological and Resources Engineering, Wuyi University, Wuyishan 354300, P. R. China
- Longhui Zheng CAS Key Laboratory of Design and Assembly of Functional Nanostructures, Fujian Key Laboratory of Nanomaterials, Fujian Institute of Research on the Structure of Matter, Chinese Academy of Sciences, Fuzhou 350002, China; orcid.org/0000-0002-6879-1414
- Jun Wang Fujian Key Laboratory of Functional Marine Sensing Materials, College of Material and Chemical Engineering, Minjiang University, Fuzhou 350108, P. R. China
- Yang Zhang Fujian Key Laboratory of Functional Marine Sensing Materials, College of Material and Chemical Engineering, Minjiang University, Fuzhou 350108, P. R. China; ⊚ orcid.org/0000-0003-0946-7910
- Zixiang Weng CAS Key Laboratory of Design and Assembly of Functional Nanostructures, Fujian Key Laboratory of Nanomaterials, Fujian Institute of Research on the Structure of Matter, Chinese Academy of Sciences, Fuzhou 350002, China; orcid.org/0000-0002-8876-2864
- Chen Zhang Fujian Key Laboratory of Functional Marine Sensing Materials, College of Material and Chemical Engineering, Minjiang University, Fuzhou 350108, P. R. China

Complete contact information is available at: https://pubs.acs.org/10.1021/acssensors.4c00916

Author Contributions

X.D., C.Z., and H.C.: conceptualization, investigation, writing—review and editing. J.X., J.X., J.Z., R.L., L.Z., J.W., Y.Z., Z.W., and L.W.: investigation and data curation.

Notes

The authors declare no competing financial interest.

ACKNOWLEDGMENTS

This work is supported by the National Natural Science Foundation of China (No. 52002162, 12174172), the Natural Science Foundation of Fujian (No. 2021J011040, 2021J05249, 2023J011396), the Scientific Research Start-up Foundation of Wuyi University (No. YJ202101), and the Fuzhou science and technology project (No. 2021-SG-273). H.C. acknowledges the support from the National Institutes of Health (award Nos. R21EB030140), the National Science Foundation (NSF) (grant Nos. 2309323, 2243979, 2319139, and 2222654), and the Penn State University.

REFERENCES

- (1) Park, S.; Heo, S. W.; Lee, W.; Inoue, D.; Jiang, Z.; Yu, K.; Jinno, H.; Hashizume, D.; Sekino, M.; Yokota, T.; Fukuda, K.; Tajima, K.; Someya, T. Self-powered ultra-flexible electronics via nano-grating-patterned organic photovoltaics. *Nature* **2018**, *561* (7724), 516–521.
- (2) Zhao, X.; Zhou, Y.; Song, Y.; Xu, J.; Li, J.; Tat, T.; Chen, G.; Li, S.; Chen, J. Permanent fluidic magnets for liquid bioelectronics. *Nat. Mater.* **2024**, 23 (5), 703–710.
- (3) Zhou, Y.; Zhao, X.; Xu, J.; Fang, Y.; Chen, G.; Song, Y.; Li, S.; Chen, J. Giant magnetoelastic effect in soft systems for bioelectronics. *Nat. Mater.* **2021**, *20* (12), 1670–1676.
- (4) Kwon, K.; Kim, J. U.; Won, S. M.; Zhao, J.; Avila, R.; Wang, H.; Chun, K. S.; Jang, H.; Lee, K. H.; Kim, J.-H.; Yoo, S.; Kang, Y. J.; Kim, J.; Lim, J.; Park, Y.; Lu, W.; Kim, T.-i.; Banks, A.; Huang, Y.; Rogers, J. A. A battery-less wireless implant for the continuous monitoring of vascular pressure, flow rate and temperature. *Nat. Biomed. Eng.* **2023**, 7 (10), 1215–1228.
- (5) Hui, Y.; Yao, Y.; Qian, Q.; Luo, J.; Chen, H.; Qiao, Z.; Yu, Y.; Tao, L.; Zhou, N. Three-dimensional printing of soft hydrogel electronics. *Nat. Electron.* **2022**, *5* (12), 893–903.
- (6) Yang, Y.; Gao, W. Wearable and flexible electronics for continuous molecular monitoring. *Chem. Soc. Rev.* **2019**, 48 (6), 1465–1491.
- (7) Mackanic, D. G.; Chang, T.-H.; Huang, Z.; Cui, Y.; Bao, Z. Stretchable electrochemical energy storage devices. *Chem. Soc. Rev.* **2020**, 49 (13), 4466–4495.
- (8) Lin, J.; Peng, Z.; Liu, Y.; Ruiz-Zepeda, F.; Ye, R.; Samuel, E. L. G.; Yacaman, M. J.; Yakobson, B. I.; Tour, J. M. Laser-induced porous graphene films from commercial polymers. *Nat. Commun.* **2014**, 5 (1), No. 5714.
- (9) Yang, Y.; Song, Y.; Bo, X.; Min, J.; Pak, O. S.; Zhu, L.; Wang, M.; Tu, J.; Kogan, A.; Zhang, H.; Hsiai, T. K.; Li, Z.; Gao, W. A laser-engraved wearable sensor for sensitive detection of uric acid and tyrosine in sweat. *Nat. Biotechnol.* **2020**, 38 (2), 217–224.
- (10) Ye, R.; Peng, Z.; Wang, T.; Xu, Y.; Zhang, J.; Li, Y.; Nilewski, L. G.; Lin, J.; Tour, J. M. In Situ Formation of Metal Oxide Nanocrystals Embedded in Laser-Induced Graphene. *ACS Nano* **2015**, *9* (9), 9244–9251.
- (11) Ren, M.; Zhang, J.; Tour, J. M. Laser-induced graphene synthesis of Co₃O₄ in graphene for oxygen electrocatalysis and metalair batteries. *Carbon* **2018**, *139*, 880–887.
- (12) Lang, X.; Hirata, A.; Fujita, T.; Chen, M. Nanoporous metal/oxide hybrid electrodes for electrochemical supercapacitors. *Nat. Nanotechnol.* **2011**, *6* (4), 232–236.
- (13) Dubal, D. P.; Ayyad, O.; Ruiz, V.; Gómez-Romero, P. Hybrid energy storage: the merging of battery and supercapacitor chemistries. *Chem. Soc. Rev.* **2015**, *44* (7), 1777–1790.
- (14) Ding, X.; Liu, R.; Zhao, J.; Hu, J.; Wu, J.; Zhang, C.; Lin, J. In situ formation of Co₃O₄ nanocrystals embedded in laser-induced graphene foam for high-energy flexible micro-supercapacitors. *Dalton Trans.* **2022**, *51* (7), 2846–2854.

- (15) Jain, R.; Lakhnot, A. S.; Bhimani, K.; Sharma, S.; Mahajani, V.; Panchal, R. A.; Kamble, M.; Han, F.; Wang, C.; Koratkar, N. Nanostructuring versus microstructuring in battery electrodes. *Nat. Rev. Mater.* **2022**, *7* (9), 736–746.
- (16) Liao, Q.; Li, N.; Jin, S.; Yang, G.; Wang, C. All-Solid-State Symmetric Supercapacitor Based on Co₃O₄ Nanoparticles on Vertically Aligned Graphene. *ACS Nano* **2015**, *9* (5), 5310–5317.
- (17) Feng, C.; Zhang, J.; He, Y.; Zhong, C.; Hu, W.; Liu, L.; Deng, Y. Sub-3 nm Co₃O₄ Nanofilms with Enhanced Supercapacitor Properties. *ACS Nano* **2015**, *9* (2), 1730–1739.
- (18) Ferrari, A. C.; Meyer, J. C.; Scardaci, V.; Casiraghi, C.; Lazzeri, M.; Mauri, F.; Piscanec, S.; Jiang, D.; Novoselov, K. S.; Roth, S.; Geim, A. K. Raman Spectrum of Graphene and Graphene Layers. *Phys. Rev. Lett.* **2006**, *97* (18), No. 187401.
- (19) Zhang, C.; Chen, H.; Ding, X.; Lorestani, F.; Huang, C.; Zhang, B.; Zheng, B.; Wang, J.; Cheng, H.; Xu, Y. Human motion-driven self-powered stretchable sensing platform based on laser-induced graphene foams. *Appl. Phys. Rev.* **2022**, *9* (1), No. 011413.
- (20) Chen, G.; Li, Y.; Bick, M.; Chen, J. Smart Textiles for Electricity Generation. Chem. Rev. 2020, 120 (8), 3668-3720.
- (21) Wen, Z.; Yeh, M.-H.; Guo, H.; Wang, J.; Zi, Y.; Xu, W.; Deng, J.; Zhu, L.; Wang, X.; Hu, C.; Zhu, L.; Xuhui, S.; Wang, Z. L. Self-powered textile for wearable electronics by hybridizing fiber-shaped nanogenerators, solar cells, and supercapacitors. *Sci. Adv.* **2016**, 2 (10), No. e1600097, DOI: 10.1126/sciadv.1600097.
- (22) Simon, P.; Gogotsi, Y. Materials for electrochemical capacitors. *Nat. Mater.* **2008**, 7 (11), 845–854.
- (23) Xu, Y.; Lin, Z.; Zhong, X.; Huang, X.; Weiss, N. O.; Huang, Y.; Duan, X. Holey graphene frameworks for highly efficient capacitive energy storage. *Nat. Commun.* **2014**, *5* (1), No. 4554.
- (24) Zhang, C.; Chen, J.; Gao, J.; Tan, G.; Bai, S.; Weng, K.; Chen, H. M.; Ding, X.; Cheng, H.; Yang, Y.; Wang, J. Laser Processing of Crumpled Porous Graphene/MXene Nanocomposites for a Standalone Gas Sensing System. *Nano Lett.* **2023**, 23 (8), 3435–3443.
- (25) Zhao, Y.; Zhang, B.; Yao, B.; Qiu, Y.; Peng, Z.; Zhang, Y.; Alsaid, Y.; Frenkel, I.; Youssef, K.; Pei, Q.; He, X. Hierarchically Structured Stretchable Conductive Hydrogels for High-Performance Wearable Strain Sensors and Supercapacitors. *Matter* **2020**, 3 (4), 1196–1210.
- (26) Zhang, C.; Peng, Z.; Huang, C.; Zhang, B.; Xing, C.; Chen, H.; Cheng, H.; Wang, J.; Tang, S. High-energy all-in-one stretchable micro-supercapacitor arrays based on 3D laser-induced graphene foams decorated with mesoporous ZnP nanosheets for self-powered stretchable systems. *Nano Energy* **2021**, *81*, No. 105609.
- (27) Zhang, C.; Huang, Y.; Tang, S.; Deng, M.; Du, Y. High-Energy All-Solid-State Symmetric Supercapacitor Based on Ni_3S_2 Mesoporous Nanosheet-Decorated Three-Dimensional Reduced Graphene Oxide. ACS Energy Lett. **2017**, 2 (4), 759–768.
- (28) Yu, D.; Goh, K.; Wang, H.; Wei, L.; Jiang, W.; Zhang, Q.; Dai, L.; Chen, Y. Scalable synthesis of hierarchically structured carbon nanotube–graphene fibres for capacitive energy storage. *Nat. Nanotechnol.* **2014**, *9* (7), 555–562.
- (29) Pech, D.; Brunet, M.; Durou, H.; Huang, P.; Mochalin, V.; Gogotsi, Y.; Taberna, P.-L.; Simon, P. Ultrahigh-power micrometresized supercapacitors based on onion-like carbon. *Nat. Nanotechnol.* **2010**, *5* (9), 651–654.
- (30) Shin, Y.; Kim, Y. W.; Kang, H. J.; Lee, J. H.; Byun, J. E.; Yang, J.-Y.; Lee, J. W. Stretchable and Skin-Mountable Temperature Sensor Array Using Reduction-Controlled Graphene Oxide for Dermatological Thermography. *Nano Lett.* **2023**, 23 (11), 5391–5398.
- (31) Sugiyama, M.; Uemura, T.; Kondo, M.; Akiyama, M.; Namba, N.; Yoshimoto, S.; Noda, Y.; Araki, T.; Sekitani, T. An ultraflexible organic differential amplifier for recording electrocardiograms. *Nat. Electron.* **2019**, 2 (8), 351–360.
- (32) Yang, L.; Wang, Z.; Wang, H.; Jin, B.; Meng, C.; Chen, X.; Li, R.; Wang, H.; Xin, M.; Zhao, Z.; Guo, S.; Wu, J.; Cheng, H. Self-Healing, Reconfigurable, Thermal-Switching, Transformative Electronics for Health Monitoring. *Adv. Mater.* **2023**, 35 (15), No. 2207742.

- (33) Niu, G.; Wang, Z.; Xue, Y.; Yan, J.; Dutta, A.; Chen, X.; Wang, Y.; Liu, C.; Du, S.; Guo, L.; Zhou, P.; Cheng, H.; Yang, L. Pencil-on-Paper Humidity Sensor Treated with NaCl Solution for Health Monitoring and Skin Characterization. *Nano Lett.* **2023**, 23 (4), 1252–1260.
- (34) Liu, Y.; Li, X.; Yang, H.; Zhang, P.; Wang, P.; Sun, Y.; Yang, F.; Liu, W.; Li, Y.; Tian, Y.; Qian, S.; Chen, S.; Cheng, H.; Wang, X. Skin-Interfaced Superhydrophobic Insensible Sweat Sensors for Evaluating Body Thermoregulation and Skin Barrier Functions. *ACS Nano* **2023**, *17* (6), 5588–5599.
- (35) Xu, Y.; Sun, B.; Ling, Y.; Fei, Q.; Chen, Z.; Li, X.; Guo, P.; Jeon, N.; Goswami, S.; Liao, Y.; Ding, S.; Yu, Q.; Lin, J.; Huang, G.; Yan, Z. Multiscale porous elastomer substrates for multifunctional on-skin electronics with passive-cooling capabilities. *Proc. Natl. Acad. Sci. U.S.A.* 2020, 117 (1), 205–213.